Elements of cellular domain patterns in magnetic garnet films

K. L. Babcock and R. M. Westervelt
Division of Applied Sciences and Department of Physics, Harvard University, Cambridge, Massachusetts 02138
(Received 24 March 1989)

Cellular patterns of magnetic domains observed in uniaxial garnet films are comprised of three elemental domain structures: stripe segments, threefold vertices that join these segments, and pentagonal structures that join five segments and contain trapped magnetic bubbles. We report observations of the stability and dynamics of these structures and show how they govern the evolution of cellular patterns in an external bias field H_B. Energy localized in the stripe segments acts as tension that drives the domain motion. A simple extension of the conventional model of stripe domains incorporates domain interactions in sparse patterns and gives access to the bias and configuration dependence of the stripe tension. We apply this formulation to an array of stripe domains to characterize the tension that arises in nonequilibrium patterns. Comparison with experiment indicates that sparse, disordered (mazelike) stripe patterns maintain equilibrium as H_B is monotonically increased and shows the expected divergence in stripe spacing at $H_B = H_{RI}$, where H_{RI} is the run-in field for isolated stripe domains. In contrast, cellular patterns persist to $H_B > H_{RI}$, where the patterns are far from equilibrium. Vertex propagation is observed when the tensions in the adjoining stripe segments are unbalanced and leads to a reduction in total stripe length and cell density. The vertices are destroyed at a critical bias field H_V ($=0.79\times 4\pi M = 151$ Oe for our garnet sample) when the stripes are severed near the vertices. H_V is the saturation field for cellular patterns and is significantly larger than that of any other observed domain configuration. Pentagonal bubble traps are also mobile and are destroyed by the collapse of the trapped bubble. A divergence of the average cell area which is limited by coercive friction occurs at the collapse field H_5 ($=0.54\times 4\pi M = 103$ Oe) of an isolated bubble trap. Nonequilibrium cellular states arise in the regime $H_{RI} < H_B < H_5$ when bubble traps resist collapse and obstruct the topological evolution. Coercive drag on the domain motion also results in nonequilibrium configurations and in some cases alters the pattern topology. We employ an ac field component to mitigate the effects of coercivity, and find that an amplitude several times larger than the coercive field H_c is required to produce smooth dynamics and ensure reproducible, metastable, stationary states.

I. INTRODUCTION

The utility of uniaxial garnet films as magnetic bubble memories and magneto-optic devices[1,2] has spawned an extensive study of the simpler domain structures which they support. The stability and dynamics of magnetic bubbles[3,4] and domain walls[5] are well understood, and the equilibrium configurations of idealized lattices of stripes, bubbles, and hexagonal cellular domains have been numerically calculated.[6–8] Nonetheless, garnet films of large lateral dimensions constitute a rich and experimentally accessible system that is far from exhausted. The two-dimensional patterns of magnetic domains observed in these films show a wide range of nonlinear behavior and disorder. Examples include the "annealing" of granular structures in arrays of magnetic bubbles by an agitating ac magnetic field,[9] and a hysteretic undulation instability of stripe patterns in a slowly cycled bias field.[10,11]

Cellular patterns are unique among garnet domain configurations in that they tend to disorder when a spatially uniform bias field H_B is monotonically increased in magnitude. We have observed two distinct room-temperature disordering mechanisms: a homogeneous coarsening and topological disordering analogous to the evolution of two-dimensional soap froths[12–14] and to the annealing of polycrystalline materials;[15,16] and a dramatic "melting" transition, shown in the photograph in Fig. 1, wherein the advance of a well-defined front destroys an ordered lattice of hexagonal domains and leaves behind a disordered cellular phase characterized by a wide diversity in the cell areas, shapes, and coordination numbers. For certain ranges of bias field, the cellular patterns are far from energetic equilibrium, and exhibit interesting dynamics and long settling times as they seek stationary states.

We have succeeded in characterizing this behavior by examining the components of the cellular patterns individually. A typical cellular configuration in a uniform bias field H_B is shown in the photograph in Fig. 2. Three elemental domain structures are seen to comprise the pattern: stripe segments, consisting of reversed magnetization (oriented opposite to H_B); threefold vertices that join these segments, thereby dividing the garnet into polygon-

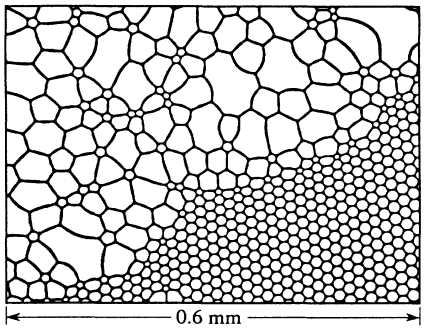

FIG. 1. Digitized photograph of a cellular "melting" transition; $H_B = 73$ Oe. White regions correspond to "up" magnetization aligned with H_B; dark regions signify reversed magnetization. The stressed lattice of hexagonal domains is formed by application of the bias field to an ordered bubble "sea" so as to expand the bubbles. The lattice is destroyed by motion of the front that separates it from the disordered cellular phase. The advance of the front is mediated by the collapse of the pentagonal bubble traps that line its length.

like cellular regions; and pentagonal domain structures which terminate five stripe segments and contain trapped bubbles. A sufficiently great bias field reduces the reversed magnetization which constitutes these structures to a small fraction of the total, and the cell boundaries reside on a background of "up" magnetization. The structures are mobile and robust: they propagate in response to motive forces, and their shape is not significantly distorted by local magnetic field perturbations. Many features of cellular pattern evolution are governed by the localized properties of these three structures. For example, energy in the stripe segments acts as tension that drives the motion of the domains, the pentagonal bubble traps obstruct the topological evolution thereby pushing the patterns far from energetic equilibrium, and the saturation field of cellular patterns is determined by the destruction of the vertices. In this paper we describe observations of the formation and dynamics of these domain structures, their response to changes in bias field, and the instabilities that destroy them. We also relate the localized properties of these structures to the frothlike disordering and "melting" transitions described above; the overall properties of these transitions will be addressed in greater detail in future papers.

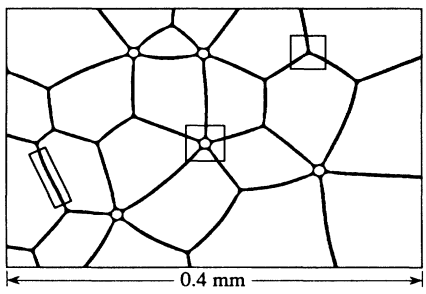

FIG. 2. Photograph of a sparse cellular domain configuration; $H_B = 90$ Oe. A stripe segment, a pentagonal bubble trap, and a threefold vertex are framed, left to right. As described in the text, this configuration is not in equilibrium; $H_B > H_{RI} = 83.5$ Oe, and there is tension in the stripe segments. This stationary pattern is characterized by a balance of the tensions at the vertices and bubble traps where the stripe segments join. Note that the trapped bubbles are comprised of magnetization aligned with H_B.

In order to provide a framework in which to discuss our observations, we will review the conventional model of stripe domain structure, and extend the model to include domain interactions in sparse patterns. In this formulation, the excess energy in nonequilibrium patterns naturally arises as tension localized in the stripe segments which governs the evolution and the stationary configurations of both stripe and cellular patterns. For example, stripe tension favors the reduction of total stripe length, and drives the frothlike coarsening and topological disordering in cellular patterns in a slowly increasing bias field. Furthermore, the metastable cellular patterns observed in certain bias regimes are characterized by a balance in the tensions of the stripe segments adjoining each of the vertices and bubble traps. This picture connects the physics of cellular domain patterns to that of soap froths, polycrystalline materials, and other cellular systems[13] whose dynamics are driven by the free energy contained in the cell boundaries.

The extension of the conventional stripe model developed below accounts for the essential effects of domain interactions by incorporating the "stray" fields of reversed domains. The behavior of individual domain structures is determined by the interplay between H_B and the stray fields, which makes the analysis of most realistic domain configurations extremely difficult. However, a parallel array of stripes provides a useful vehicle with which to extract the important properties of the stripe tension. The energies and minimum energy configurations of a sparse stripe array are readily determined, and aid in the comparison of observations of cellular patterns and disordered (mazelike) stripe patterns. They also provide a reference useful for characterizing the bias and configuration dependence of the tension in stripe segments embedded in nonequilibrium cellular patterns. We note that the stripe-array energies as determined here are approximate for all but the sparsest patterns,[7] and that the exact equilibrium energies and configurations of idealized stripe arrays have been evaluated previously[6–8] for the entire range of bias field. However, the stripe tension is a useful and intuitive concept that does not readily emerge from exact treatments of stripe arrays, and the formulation described in this paper gives access to properties of the tension that are relevant to cellular patterns as well.

An additional topic discussed here is the role of coercivity in the evolution of domain patterns, a property of the garnet that creates frictional drag on the motion of

the domain walls.[5] Coercivity impedes the ability of the patterns to reach stationary states which correspond to local energy minima in the space of domain configurations. We employ an ac field in addition to the dc bias to mitigate coercive effects and help the patterns attain these metastable states. An ac field of appropriate frequency and sufficient amplitude results in smooth dynamics of the domain structures which, in certain bias regimes, are strikingly similar to those of soap froths.[13,14] The required amplitude is surprisingly large, i.e., several times larger than the coercive field itself. An inadequate ac amplitude can result in uneven domain motion, the anomalous severing of the stripe segments as the patterns evolve, the formation of stationary states dominated by friction, and loss of reproducibility.

The remainder of the paper is organized as follows. In Sec. II we discuss the relevant material properties of the garnet, briefly review the conventional model of domain walls, and describe the methods used to influence and observe the domains. The structure of stripe domains is reviewed in Sec. III to elucidate their robust nature and the bias dependence of the stripe energy. This treatment is extended in Sec. IV to show how the stripe properties are modified by domain interactions. We characterize nonequilibrium patterns by examining the configuration and bias dependence of the stripe tension in a parallel stripe array, and compare observations of stripe and cellular patterns. Section V describes the propagation of the vertices and their destruction via stripe pinch-off. The formation of the pentagonal bubble traps, their destruction via the collapse of the trapped bubble, and their role in the frustration of the topological evolution are described in Sec. VI. Finally, we discuss the influence of coercivity on the dynamics of stripe segments in Sec. VII, and show that a large ac-field component is necessary to mitigate coercive effects. The relation of these properties to the overall cellular evolution in an increasing bias field is described throughout the paper and in a concluding discussion.

II. MATERIAL CHARACTERISTICS AND DOMAIN STRUCTURE

The sample used for our observations is a bismuth-substituted iron garnet film with material composition $Fe_{3.91}Y_{1.20}Bi_{1.09}Gd_{0.95}Ga_{0.76}Tm_{0.09}O_{12}$ formulated at the Airtron Division of Litton Industries[17] for use in magneto-optic devices. The film was grown by liquid-phase epitaxy to a thickness of 7.8 μm on a nonmagnetic substrate of matching lattice constant, and has a usable area of several cm^2 with low defect density. The bulk magnetization is $4\pi M = 190$ G, as determined by optical measurement of stripe domain widths, and the Curie point is 170 °C. All parameters given are valid for room temperature, at which our observations are made.

The strong uniaxial anisotropy of the Airtron garnet is measured by its quality factor:[1,5] $Q = K_u / 2\pi M^2 = 11.1$, where K_u is the uniaxial anisotropy parameter,[1,5] M is the bulk magnetization, and the denominator is the energy density of a standard (single domain) garnet. A Q larger than unity precludes the formation of closure domains containing magnetization aligned with the film plane, and the magnetization is predominantly oriented perpendicular to the film plane. The thickness of the domain walls is approximately 0.1 μm; over this region the magnetization changes continuously from "up", or aligned with the bias field, to "down", or reversed. The domain-wall thickness is negligible compared to the typical domain size, and the patterns are essentially two dimensional. At low velocities,[5] domain-wall motion occurs by rotation of the magnetization that translates the wall laterally while preserving its structure.

The domain walls in device garnets are conventionally modeled[5] as infinitesimally thin and as rigidly aligned in the direction normal to the film plane; this geometry is illustrated in Fig. 3. This approximation is excellent for the high-Q Airtron garnet. The energy contained in the domain walls is effectively a surface energy σ_w, which for the Airtron garnet has a magnitude $\sigma_w = 0.23$ erg/cm^2, as we determined by conventional methods[1,5] from measurements of bubble radii and collapse fields. This "wall-energy" picture provides a useful and accurate tool for the characterization of domain structure and material parameters. For example, a standard method (used here) for inferring the magnetization and domain-wall energy is to compare observations of bubbles and stripes to predictions of the wall-energy model. Conversely, descriptions of domain structure attained from the model are useful in the design of materials appropriate for devices.[1] Our discussion of the stripe segments, vertices, and bubble traps utilizes the wall-energy picture.

Characteristic domain sizes are determined by competition between the energy contained in the demagnetization fields (those that have the magnetization as their source), and the domain-wall energy.[18] A balance in this competition is reflected by the characteristic length[1,5] $\xi = \sigma_w / 4\pi M^2$; the numerator is the domain-wall surface energy, and the denominator is proportional to the demagnetization energy density of a standard (single-domain) configuration. The length ξ is intrinsic to the material and is independent of the film dimensions, and represents the approximate domain size (e.g., bubble radius or stripe width) in a film of thickness comparable to ξ; geometrical effects result in domain sizes that are

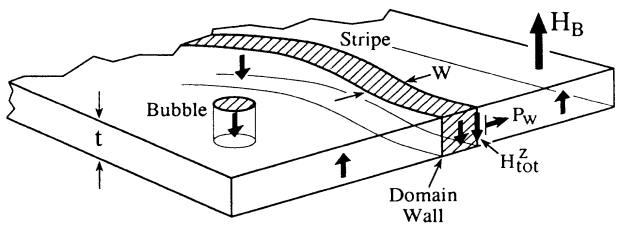

FIG. 3. Schematic of domain geometry showing idealized bubble and stripe domains comprised of reversed magnetization. The domain walls are modeled as infinitesimally thin and as rigid in the direction normal to the film plane. Also indicated is the pressure $P_w = 2MH_{tot}$ produced by a nonzero total field at a wall.

larger than ξ in films of thickness $t > \xi$. Within the context of the wall-energy picture, two garnet films with the same ratio ξ/t of characteristic length to film thickness possess identical metastable domain structures when spatial dimensions are expressed in units of film thickness t and fields are cast in units of $4\pi M$. This ratio is thus useful for comparison of domain structures in different garnet films. We have observed behavior in other garnet films with ratios $\xi/t = 0.09$ and $\xi/t = 0.13$ which is qualitatively identical to that described in this paper for the Airtron garnet, with ratio $\xi/t = 0.104$.

Motive pressure on a domain wall arises when the component of the total magnetic field normal to the film plane is nonzero at the domain-wall locations.[5] The total field is the sum of the externally applied bias field H_B, the demagnetization field H_D produced by the configuration of magnetization, and an effective "wall-energy" contribution due to the surface tension term $H_w^{\text{eff}} = \sigma_w / 2Mtr$, where r is the total radius of curvature along the wall. As illustrated in Fig. 3, the resulting pressure $P_w = 2MH_{\text{tot}}$ dyn/cm^2 favors domain wall motion in the direction that increases the amount of magnetization aligned with H_{tot}. (H_{tot} denotes the component of the total field normal to the film plane.) Opposing the motive pressure is a coercive frictional "pressure"[5] P_c originating in microscopic defects or fluctuations in material parameters, which is conventionally expressed in terms of a coercive field H_c: $P_c = 2MH_c$. The static coercive field for the Airtron garnet is in the range $H_c = 0.2$–0.5 Oe, typical for device garnets.

Metastable domain patterns, i.e., those that correspond to local energy minima in the space of domain configurations, satisfy the local condition $H_{\text{tot}} = 0$ at all domain-wall positions. The stationary configurations would satisfy this condition in the idealized case of $H_c = 0$. However, because all garnet films have nonzero coercivity, H_{tot} at the domain walls may deviate from zero by as much as H_c in the stationary domain configurations that are actually observed. Only when H_{tot} exceeds H_c does the motive pressure overcome friction and force the wall to move. In this way, coercivity acts as stick-slip friction on individual domain walls. We will show in Sec. III that coercivity has little influence on the static parameters of individual domains, such as stripe width and bubble radius. However, it produces a drag on the domain motion that can alter and even dominate the evolution and stationary states of stripe and cellular patterns.

In order to mitigate coercive effects, we apply a spatially uniform ac field in addition to the dc bias field; the total external field has the form $H_{\text{ext}} = H_B + H_{\text{ac}} \sin(2\pi\nu t)$. H_B serves as the control parameter which drives the pattern evolution, while the ac field agitates the domain walls, effectively reduces friction, and permits smooth domain motion.[19] We find that the ac amplitude must be several times larger than the coercive field H_c itself if the observed stationary states are to approach truly metastable domain configurations. For the examples in this paper where ac is employed, $\nu = 40$ Hz and $1 < H_{\text{ac}} < 5$ Oe. Coercivity and the ac field are discussed further in Sec. VII.

The domain patterns are conveniently observed with a standard metallurgical microscope by utilizing the Faraday effect. Linearly polarized light is rotated as it passes through the garnet, with a handedness that is opposite for up and down domains. An analyzer positioned between the garnet and the microscope eyepiece yields contrast between the two domain polarities. The Airtron garnet possesses a high "figure of merit" (ratio of magneto-optic rotation to absorption, per unit thickness) of 4°/dB (Ref. 17), and yields bright, high-contrast images ideal for photographic and video recording and subsequent image processing. All images of domains shown in the figures are high-resolution digitizations of high-contrast Polaroid photographs.

Many of the domain structures shown in this paper are embedded in sparse, disordered cellular patterns. To create these patterns, a disordered "sea" of magnetic bubbles (the "amorphous" structure of Ref. 9) of density 7900 bubbles/mm^2 is produced by application and removal of a 2.2-kG magnetic field that saturates the garnet in the "hard" (in-plane) direction. An increase in a bias field aligned with the bubble magnetization eliminates some bubbles and expands others, resulting in a stripe-vertex network such as that in Fig. 2.

III. STRIPE SEGMENTS

A typical response of an individual stripe segment to a cycled bias field H_B is shown in the photographs in Fig. 4. The segment is initially buckled, and straightens continuously as H_B is increased. The segment buckles when the field is subsequently reduced to its initial value. The changes in H_B are made quasistatically, i.e., slowly enough that the segment remains in metastable equilibrium at all times. The cycle is hysteretic, in that H_B must be reduced by an interval ≈ 2 Oe from the cycle maximum before the buckling is initiated. Note that the width of the stripe remains nearly constant along its length. The response can be likened to that of a string or ribbon that can be made alternately taut or limp by varying an external parameter, and whose length is not con-

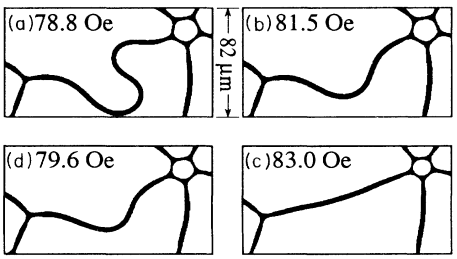

FIG. 4. Photographs showing the response of a stripe segment to a slowly cycled bias field. In frames (a)–(c), the initially buckled segment straightens continuously as H_B is increased. The segment buckles [frame (d)] when the field is subsequently reduced. The ends are anchored at a vertex and a pentagonal bubble trap. An ac-field component ($H_{\text{ac}} = 2.5$ Oe, $\nu = 40$ Hz) is present throughout.

served. The particular stripe segment shown is embedded in a sparse cellular pattern, with the ends anchored to a vertex and pentagonal bubble trap which remain nearly stationary throughout the cycle. This buckling-straightening response is also typical of individual stripes in sparse stripe patterns and of isolated stripe segments with ends pinned at defects.

This behavior can be understood by examining the dependence of stripe width and energy on H_B as described by the wall-energy model. We review the analytically tractable case of an idealized, infinite stripe with geometry similar to that of Fig. 3, but with straight domain walls. The z (film normal) component $H_{\rm tot}$ of the total magnetic field, evaluated at the domain walls and averaged over the film thickness t, is the sum of the bias field H_B and the averaged demagnetization field

$$\langle H_{\rm tot}^{\rm wall}\rangle_t = H_B - 4\pi M + \langle H_{\rm D}^{\rm self}(w)\rangle_t \ , \tag{1}$$

where a positive sign signifes alignment with H_B. The demagnetization contribution is the sum of the value $-4\pi M$ for a saturated (stripe absent) state and a "self"-correction $H_D^{\rm self}(w)$ due to the reversed magnetization in the stripe. The average over the film thickness t is required by the wall-energy model approximation that treats domain walls as vertically rigid. We assume this average in future expressions of the demagnetization field. The averaged self-field of the straight, infinite stripe is[6,20]

$$H_{\rm D}^{\rm self}(w) = 8M\left\{\tan^{-1}\left[\frac{w}{t}\right] + \frac{w}{2t}\ln\left[1+\left[\frac{t}{w}\right]^2\right]\right\} . \tag{2}$$

The stripe width w_s is determined by the requirement that the pressure $P_w = 2MH_{\rm tot}^{\rm wall}$ on the individual stripe walls be zero. This condition represents a balance between the bias field, which favors narrowing the stripe, and the total demagnetization field, which prefers to widen it. Figure 5 shows the widths w_s in units of thickness t versus H_B in units of $4\pi M$ which satisfy $H_{\rm tot}^{\rm wall}(w, H_B) = 0$, determined by using Eqs. (1) and (2). We find experimentally that the width of stripe domains closely follows Fig. 5 when the domains are well separated. The calculated width w_s in Fig. 5 vanishes for $H_B > 1$ ($H_B > 4\pi M$ Oe). For a given value of H_B, a deviation of the stripe width from the value w_s of Fig. 5 alters $H_D^{\rm self}(w)$ and produces a nonzero total field at the stripe walls. The result is a restoring pressure that opposes such deviations. However, nonzero coercivity allows $H_{\rm tot}$ to differ from zero by as much as H_c before the wall width must adjust. The maximum deviation $|\Delta w|$ in the observed width from w_s due to coercivity is thus approximately $|\Delta w| = |(\partial w_s/\partial H_B)H_c|$. Evaluating the derivative of w_s at intermediate values of H_B where isolated stripes are observed and using the (conservative) value $H_c = 0.5$ Oe, gives $|\Delta w| < 0.01 w_s$. Thus we can conclude that coercivity does not significantly hinder the ability of the observed stripe width to obey the wall-energy model result w_s of Fig. 5. Note that because w_s is determined by the condition $H_{\rm tot} = 0$, Fig. 5 is also a plot of the component of the total demagnetization field H_D aligned opposite to H_B versus stripe width w_s. The relatively weak dependence of w_s on H_D for $H_B \gtrsim 0.3$ implies that the width is insensitive to perturbations in the demagnetization field that occur when the stripe is buckled or when the stray fields of other reversed domains alter the field configuration. This robustness contributes to the ribbon-like nature of stripes when curved or embedded in a pattern.

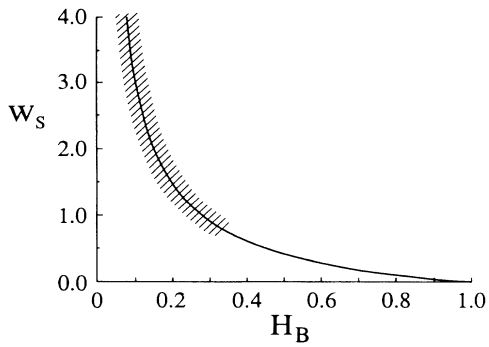

FIG. 5. Width w_s of an isolated stripe vs bias field in units of film thickness t and magnetization $4\pi M$, respectively. The hatching signifies the range of H_B where domains densely populate the garnet and stripes are difficult to observe in isolation.

The stripe energy per unit length can be obtained by integrating the virtual work done by lateral domain wall pressure $P_w = 2MH_{\rm tot}^{\rm wall}$ as the stripe width is increased from zero and adding the wall-energy contribution:

$$E_s = \int_0^{w_s} 2MtH_{\rm tot}^{\rm wall}(w)\,dw + 2t\sigma_w \ \ \text{ergs/cm} \tag{3a}$$

$$= H_B w_s - \frac{w_s}{2\pi}\left[4\tan^{-1}\left[\frac{1}{w_s}\right] - \left[w_s - \frac{1}{w_s}\right]\times\ln(1+w_s^2) + 2w_s\ln(w_s)\right] + \frac{\xi}{t} \ , \tag{3b}$$

where we have used Eqs. (1) and (2), evaluated the integral, and changed to dimensionless units: lengths are expressed in units of film thickness t, fields in units of $4\pi M$, and the energy per unit length in units of $8\pi M^2 t^2$. The first term in Eq. (3b) is the interaction energy of the stripe magnetization with the bias field, the second is the energy contained in the demagnetization fields, and ξ/t is the dimensionless expression of the domain-wall energy contained in both walls of the stripe. All energies are measured relative to the energy of the saturated (stripe absent) state, an energy reference which varies with H_B.

The total energy per unit length E_s of the idealized stripe is plotted in Fig. 6, as given by Eq. (3b) evaluated with the Airtron garnet parameters. The maximum value of E_s is attained at $H_B = 1$ ($H_B = 4\pi M$ Oe), where $w_s = 0$ and the only contribution to E_s is the energy ξ/t of the

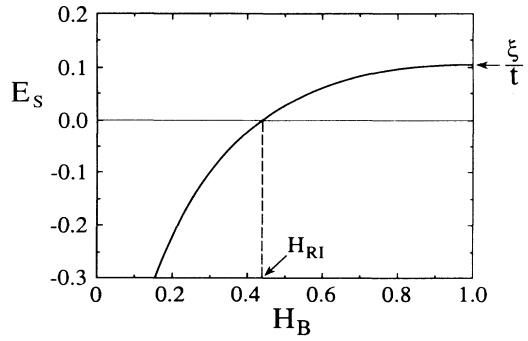

FIG. 6. Energy per unit length E_s of an isolated stripe domain in units of $8\pi M^2 t^2$ vs bias field in units of $4\pi M$, from Eq. (3b). The zero crossing corresponds to the run-in field H_{RI}, at which the stripe tension is zero. ξ/t is the energy contained in the two domain walls.

two domain walls. The zero crossing at $H_B = 0.44 \times 4\pi M = 83.5$ Oe is referred to as the "run-in" field H_{RI},[5,7] because the free ends of a finite, unconnected stripe are observed to run in along the stripe length when H_B is increased above this value, thereby reducing the total energy.

The behavior of a curved stripe segment with no free ends, such as the one shown in Fig. 4, suggests that the positive energy E_s for $H_B > H_{RI}$ in Fig. 6 acts as a tension $T_s = E_s$ in the stripe. There is an effective lateral pressure [(force)/(length)] on a curved segment of the stripe of magnitude $P_s = T_s / r_s$, where r_s is the local radius of curvature. When $P_s > 0$, the stripe is induced to straighten and thereby reduce its length and energy, whereas $P_s < 0$ favors an increase in length via buckling. While the motive pressure P_w acts on the individual domain walls, P_s and T_s effectively act on the stripe as a whole because the width is strongly constrained, as discussed above. Note that the motive force on a curved stripe segment is controlled by the spatially uniform bias field, and does not result from gradients in the external field or in the demagnetization fields of interacting domains.

We emphasize that the magnitude of T_s is determined by the total stripe energy, and not the domain-wall energy alone. Tension in stripe segments is the dominant driving force in the evolution of both cellular and stripe patterns in an increasing bias field. T_s induces the movement of stripe segments that constitute the cell walls in cellular patterns, and plays a role analogous to the surface energy of bubble membranes in soap froths and of grain boundaries in polycrystalline materials. Because $T_s \leq 2\sigma_w t$ erg/cm, the pressure T_s / r_s is always smaller than the total surface tension pressure $2\sigma_w t / r_s$ of the two domain walls of the stripe. The pressure T_s / r_s is, in fact, typically much smaller for stripe segments observed in sparse patterns, and coercive effects can become important. Coercivity may, for example, play a role in the hysteretic buckling in Fig. 4. We will come back to this point in Sec. VII.

IV. STRIPE TENSION AND NONEQUILIBRIUM PATTERNS

In this section we extend the treatment of the isolated stripe to account for domain interaction in sparse patterns. Reversed domains interact via their stray fields in two ways. One is that gradients in the stray fields produce mutual domain repulsion which favors, for example, the ordering of magnetic bubbles into lattices[9] and the uniform spacing observed in stripe patterns. The second is that the stray field originating in a given reversed domain adds to the influence of the bias field on other reversed domains. The latter effect is accounted for by including the contribution of the stray fields to the demagnetization field, and the width and energy of an individual stripe embedded in a pattern can be determined as in Sec. III. Analytic results are difficult to obtain for even the simplest cellular configurations. However, the most important effects of domain interactions on both cellular and stripe patterns can be usefully and conveniently illustrated by examining a parallel array of stripe domains. The equilibrium configuration of the array is readily determined using the dipole expressions for the stray fields of stripe domains. The results preserve the important features of previous exact calculations,[6-8] and agree favorably with experimental observations of sparse, disordered (mazelike) stripe patterns in a monotonically increased bias field. Most importantly, the energy of the stripes in the minimum-energy array configuration provides a benchmark for outlining the bias regimes in the evolution of both stripe and cellular patterns, and for characterizing the bias and spacing dependence of the stripe tension which arises in nonequilibrium patterns.

We proceed as in Sec. III, and focus on the fields experienced by an individual stripe segment in the pattern. The normal component of the total field at a domain wall of this stripe now has the form $H_{\rm tot}^{\rm wall} = (H_B + H_D^{\rm dip}) - 4\pi M + H_D^{\rm self}$. The contributions of other reversed domains are included in $H_D^{\rm dip}$, which denotes the dipole approximation of the stray fields. $H_D^{\rm dip}$ varies with the domain spacing, but is approximated as spatially uniform across the width of the specified stripe and through the thickness of the film. The expression in parentheses thus acts as a corrected "bias" field. To evaluate $H_D^{\rm self}$ we retain the self-demagnetization field of a straight, infinite stripe as given by Eq. (2). The width and energy per unit length of the stripe can then be found as in Sec. III. This general formulation can, in principle, describe individual stripe segments in patterns with various degrees of disorder, and in patterns that contain domain structures other than stripes (e.g., bubbles or vertices), so long as $H_D^{\rm dip}$ is evaluated appropriately.

Within this framework, we can readily calculate the width and energy of a stripe in the parallel array illustrated in Fig. 7, which shows stripes (shaded) of uniform width w and spacing d. Also sketched are the stray field lines of the outer stripes, showing that they add to H_B at the center stripe. The dipole field of a straight, infinite stripe is given by $2Mtwx^{-2}$, where Mtw is the dipole moment per unit length, and x is the perpendicular distance

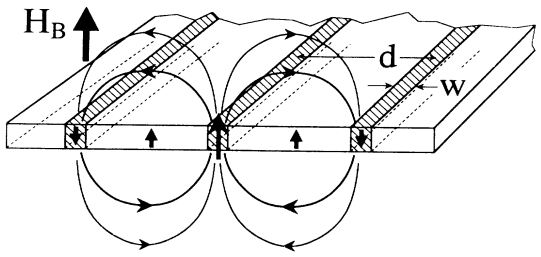

FIG. 7. Parallel array of stripe domains. The outer two stripes produce stray fields (sketched) that add to the influence of H_B on the central stripe.

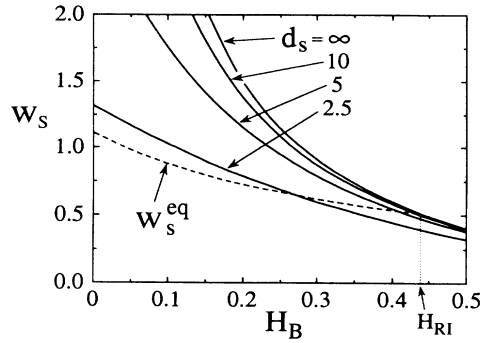

FIG. 8. Widths w_s of stripes vs bias field in units of film thickness and $4\pi M$, respectively, as calculated for the parallel array. The solid curves are for various fixed-stripe spacings d_s, from Eq. (5). The dashed curve shows the stripe widths of the equilibrium configurations. The widths at finite spacing are reduced relative to the isolated stripe ($d_s=\infty$) case due to the enhancement of H_B by the stray fields.

from the stripe. This expression is accurate for distances x much greater than both the film thickness and the typical domain size. The total stray field contribution at a given stripe due to all other stripes is

$$H_D^{\rm dip}(w,d)=2\sum_{n(\neq 0)} 2Mtw(nd)^{-2}=C^{\rm arr}Mtw\,d^{-2}\ , \quad (4)$$

where the constant $C^{\rm arr}=(4/3)\pi^2$ is specific to the array geometry. The leading factor of 2 accounts for the requirement that reversed magnetization of magnitude $2M$ must be superimposed on the saturated garnet to obtain stripes of reversed magnetization M.

As before, the stripe widths w_s (H_B,d) for fixed separation d are determined by the condition $H_{\rm tot}=0$:

$$H_{\rm tot}^{\rm wall}(H_B,d,w)=(H_B+C^{\rm arr}Mtwd^{-2})-4\pi M + H_D^{\rm self}(w)=0\ , \quad (5)$$

where $H_D^{\rm self}$ is given by Eq. (2). The form of Eq. (5) shows that the stray-field contribution serves to augment the bias field, as illustrated in Fig. 7. The solid curves in Fig. 8 show the stripe widths $w_s(H_B,d)$ which satisfy Eq. (5) for various fixed-stripe spacings d. As shown, the widths at finite spacing are reduced relative to the isolated stripe ($d\to\infty$) limit because of the enhancement of the bias field by the stray fields. For fixed H_B, the influence of the stray fields is reduced as the separation increases, and w_s increases accordingly. Note that, as before, the stripe width is highly constrained due to strong restoring forces on the domain walls, whereas the interdomain forces that affect the stripe spacing are much weaker. In what follows, Eq. (5) is assumed to be satisfied.

The energy per unit area in the stripe array can be expressed as $E_A^{\rm arr}=E_s^{\rm arr}(H_B,d)d^{-1}$, where $E_s^{\rm arr}$ is the energy per unit length localized in each stripe, and d^{-1} is the linear stripe density. By holding the spacing d fixed, the energy $E_s^{\rm arr}$ can again be found by integrating the virtual work performed by the wall pressure P_w as the stripe width increases from zero. Domain interactions are accounted for by including the dipole fields $H_D^{\rm dip}$ in $H_{\rm tot}$ and by using the width $w_s(H_B,d)$ determined by Eq. (5) as the upper limit of the integral

$$E_s^{\rm arr}(H_B,d)=\int_0^{w_s(H_B,d)}2MtH_{\rm tot}^z(H_B,d,w)dw + 2t\sigma_w \ {\rm erg/cm}\ , \quad (6a)$$

$$=E_s^{\rm isol}(H_B,w_s(H_B,d))+\frac{C^{\rm arr}}{2}\left[\frac{w_s(H_B,d)}{d}\right]^2\ , \quad (6b)$$

where $E_s^{\rm isol}$ is the energy per unit length of an isolated stripe as given by Eq. (3), evaluated with the stripe width determined by Eq. (5). In Eq. (6b), lengths are in units of t, fields in units of $4\pi M$, and energies in units of $8\pi M^2t^2$; the geometrical constant $C^{\rm arr}=\pi/3$ in these units.

For a fixed bias field, the equilibrium[21] (minimum-energy) array configuration is determined by minimizing $E_A^{\rm arr}$ with respect to w and d, simultaneously. This is simply done by solving for $d(w)$ using Eq. (5) and inserting the result into the expression for $E_A^{\rm arr}$ obtained from Eq. (6b) to give

$$d(H_B,w)=\left[\frac{C^{\rm arr}w}{1-[H_D^{\rm self}(w)+H_B]}\right]^{1/2}\ , \quad (7a)$$

$$E_A^{\rm arr}(H_B,w)=[d(H_B,w)]^{-1}\{E_s^{\rm isol}(H_B,q) + w[1-(H_D^{\rm self}(w)+H_B)]\}\ , \quad (7b)$$

with $H_D^{\rm self}$ given by Eq. (2) and $E_s^{\rm isol}$ by Eq. (3). After inserting these expressions and rearranging, Eq. (7b) becomes

$$\sqrt{C^{\rm arr}}E_A^{\rm arr}(H_B,w) = \left[\frac{2}{\pi w}\tan^{-1}\left[\frac{1}{w}\right]-\frac{1}{\pi}\ln\left[\frac{1+w^2}{w^2}\right]-\frac{H_B}{w}\right]^{1/2} \times\left[\frac{\xi}{t}+\frac{H_Bw}{2}-\frac{w}{\pi}\tan^{-1}\left[\frac{1}{w}\right]-\frac{1}{2\pi}\ln(1+w^2)\right]\ . \quad (8)$$

Numerically minimizing this expression with respect to w yields the equilibrium energy $E_A^{eq}(H_B)$ and stripe width $w_s^{eq}(H_B)$. The equilibrium width is plotted in Fig. 8 as the dashed curve. As expected, w_s^{eq} is smaller than the width of an isolated stripe, due to the stray field enhancement of H_B, and approaches the isolated stripe value as $H_B \rightarrow H_{RI}$.

The equilibrium stripe separation $d_s^{eq}(H_B)$ is obtained for the parallel array by inserting w_s^{eq} into Eq. (7a). The separation $d_s^{eq}(H_B)$ is shown in Fig. 9 as the solid curve; also plotted are the average stripe spacings $\langle d_s \rangle$ (described below) experimentally observed in disordered stripe patterns. Although the widths w_s^{eq} remain finite, the equilibrium separation d_s^{eq} diverges as $H_B \rightarrow H_{RI}$, because for $H_B > H_{RI}$ each stripe in the array has positive energy relative to the saturated configuration. The divergence obeys $d_s \propto (H_{RI} - H_B)^{-\beta}$ with the exponent $\beta \approx \frac{1}{2}$, as can be seen from the form of Eq. (7a). The results d_s^{eq} in Fig. 9 overestimate the equilibrium spacings given by exact treatments[6–8] of the stripe array. However, the agreement is excellent for large stripe spacings where the dipole expressions of the stray fields are valid, and for our purposes the present calculation is adequate.

The data points in Fig. 9 indicate the average stripe spacings $\langle d_s \rangle$ observed in disordered (mazelike) stripe patterns evolved under a slowly, monotonically increased bias field. An ac field component was also applied to minimize coercive effects. Such stripe patterns are readily produced by reducing H_B from saturation: the free ends of a few stripes nucleated at the garnet edges run in and fill the garnet, producing the zero-field pattern shown in the first photograph of Fig. 9. Other photographs in the sequence show the patterns that result at selected intervals of increasing H_B. We measured the length of domain wall per unit garnet area, l_A^{wall}, by computer analysis of high-resolution digitizations of high-contrast photographs. The average stripe spacing was then determined as $\langle d_s \rangle \equiv 2/l_A^{wall}$. This relation is exact for an ordered stripe array, and is also reasonably accurate for the patterns in Fig. 9, which show a fairly uniform stripe spacing caused by the mutual repulsion of the stripes. The experimental values shown as data points in Fig. 9 agree well with the equilibrium spacings $d_s^{eq}(H_B)$ calculated above for the idealized array, shown as the smooth curve. The observed stripe spacing $\langle d_s \rangle$ exhibits the expected divergence at H_{RI}. However, the divergence is limited by the presistence of a few strips due to coercive effects and the pinning of the stripe ends at the garnet edges. Over the limited range of H_B (~ 10 Oe) for which the algebraic form holds experimentally, the exponent is $\beta = 0.49 \pm 0.02$.

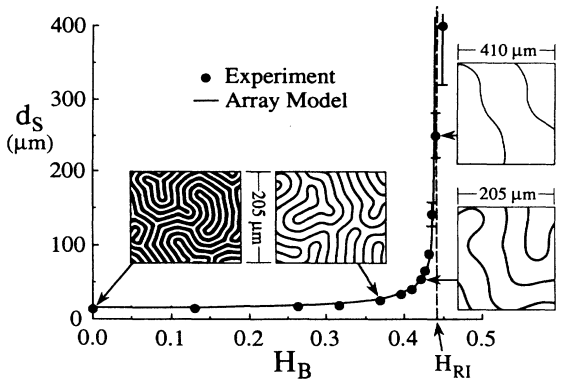

FIG. 9. Stripe spacing d_s (μm) vs bias field (units of $4\pi M$), showing the divergence of d_s at $H_B = H_{RI}$. The solid curve is the equilibrium spacing $d_s^{eq}(H_B)$ calculated for the idealized stripe array. The data points are the average stripe spacing observed in disordered (mazelike) stripe patterns in a slowly, monotonically increased bias field. The photographs show these patterns at selected bias values. The uppermost data point indicates the persistence of a few stripes to $H_B > H_{RI}$ due to coercivity and pinning of stripe ends at the garnet boundaries. Error bars represent the standard deviation in d_s as measured for three different areas on the garnet surface. As ac field ($H_{ac} = 5$ Oe, $\nu = 40$ Hz) was applied to minimize coercive effects.

The agreement of the observed stripe spacing $\langle d_s \rangle$ with the minimum-energy values d_s^{eq} of the idealized array indicates that there are few barriers to the evolution of the disordered stripe patterns which prevent them from maintaining equilibrium as H_B is increased. As can be seen from the photographs in Fig. 9, the stripes in these patterns increase their averaging spacing by uncoiling and reducing their curvature and total length as H_B increases, while keeping the spacing fairly uniform along the lengths of the stripes. Furthermore, if a sufficient ac field component is present to mitigate coercive friction, the stripe pattern evolution is almost completely reversible: the patterns "coil up" and decrease the average stripe spacing in response to a decrement in H_B, with little hysteresis. The coiling-uncoiling mechanism of spacing adjustment allows the stripe patterns to maintain equilibrium as H_B is increased. In contrast, nonequilibrium cellular patterns are formed when pentagonal bubble traps inhibit the topological evolution, as described in Sec. VI.

The equilibrium (minimum-energy) configuration determined above for the parallel stripe array provides a useful reference for characterizing deviations from equilibrium in both stripe and cellular patterns. Much of the excess energy in nonequilibrium patterns (those that are not of minimum energy) is localized as tension in the stripes that attempts to drive the patterns toward equilibrium. Evaluating the bias field and stripe spacing dependence of the tension for a nonequilibrium, parallel stripe array illuminates the mechanisms that result in nonequilibrium cellular patterns. A simple and useful generalization of the stripe tension in the parallel array is

$$T_s(H_B,d) \equiv E_s(H_B,d) - E_s^{eq}(H_B) , \tag{9}$$

where E_s is the energy per unit length localized in each stripe as given by Eq. (6b), and E_s^{eq} is the value of E_s in the minimum-energy array configuration determined above. This definition is such that nonzero tension T_s results whenever the array deviates from the equilibrium configurations. We focus on the spacing and bias depen-

dence of T_s, and assume that the stripe width obeys $w(H_B,d)$ given by Eq. (5). Equation (9) can be evaluated by inserting $w(H_B,d)$ into Eq. (6b); the tension T_s versus spacing d for various fixed H_B is shown in Fig. 10. The zero crossings for each field value correspond to the equilibrium stripe separations $d_s^{eq}(H_B)$. Because the divergence of $d_s^{eq}(H_B)$ at H_{RI} leaves the saturated state as the energy reference for $H_B > H_{RI}$, $T_s > 0$ for stripes in this bias regime, independent of the spacing.

Figure 10 also illustrates the response of a stripe array that maintains the equilibrium (minimum energy) as H_B is increased. Assume that the array is initially in equilibrium at $H_B = 0.40$. An increment in H_B of magnitude 0.2 is indicated by the first arrow, which leads to the curve valid for the new bias value. The tension becomes positive in the stripe segments, and the pattern adjusts by increasing the stripe spacing until equilibrium is reestablished, as indicated by the second arrow. Note that positive tension would remain if d_s were unable to increase sufficiently. Inhibited spacing adjustment is the most common mechanism by which nonequilibrium states arise in both stripe and cellular domain patterns under increasing bias. In the case of disordered stripe patterns, tension created when H_B is incremented drives the observed uncoiling and the corresponding spacing increase. Only for $H_B \approx H_{RI}$ do stripe patterns deviate from equilibrium when coercivity (Sec. VII) prevents the stripes from uncoiling sufficiently.

The tension T_s in the stripe array from Eq. (9) is shown in Fig. 11 versus H_B for various fixed-stripe spacings d_s. The values of H_B at the zero crossings play a role analogous to that of the run-in field H_{RI} for an isolated stripe, in that T_s switches between positive and negative at these values in arrays of corresponding spacing. Note that the zero-tension fields in Fig. 11 increase with the stripe spacing d_s, due to the corresponding reduction in the strength of the stray fields. These properties of the tension are consistent with our observations of stripe segments embedded in cellular patterns. As shown in the example of Fig. 4, individual segments respond to a cycled bias field by alternatively buckling and straightening while other reversed domains remain fixed. The values of the bias at which the tension appears to pass through zero are smaller than H_{RI}, and increase as the pattern becomes more sparse.

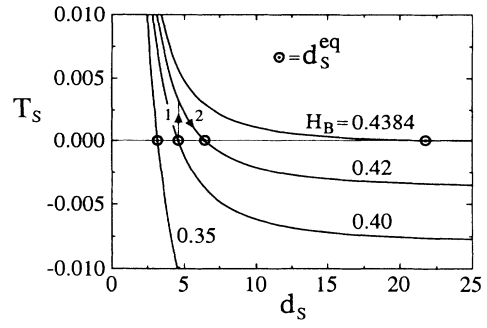

FIG. 10. Stripe tension T_s vs spacing d_s (units of $8\pi M^2 t^2$ and film thickness, respectively) for various fixed-bias fields, as determined for the parallel array using Eq. (9). The zero crossings correspond to the equilibrium spacings $d_s^{eq}(H_B)$, which diverge at $H_B = H_{RI} = 0.44$. When $H_B > H_{RI}$, any existing stripes are under positive tension, regardless of spacing. The response of a pattern to an increment in H_B is shown by the arrows. The first indicates a bias increase from $H_B = 0.40$ to 0.42 that produces tension in the pattern. In this example, equilibrium is reestablished by an increase in stripe spacing, as shown by the second arrow.

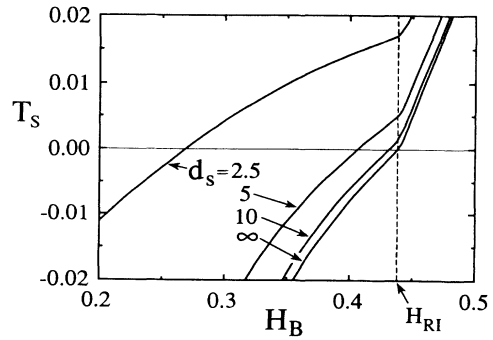

FIG. 11. Stripe tension vs bias field (units of $8\pi M^2 t^2$ and $4\pi M$, respectively) calculated for the parallel array using Eq. (9), for various fixed spacings d_s. Note that the zero crossing bias increases with d_s. Positive tension in the stripe segments is prevalent in nonequilibrium patterns which cannot maintain a sufficiently large spacing as H_B is increased. The discontinuity in the slope of T_s at $H_B = H_{RI}$ is due to the change in the energy reference used to define T_s.

The conclusion that stripe domains have positive tension for $H_B > H_{RI}$ applies to stripe segments in cellular patterns as well as to stripe arrays, as can be seen by considering the limit of low cell density. The stripe segments that constitute the cell walls become arbitrarily long in this limit, and their tension approaches that of an isolated stripe. Energetics thus dictate that the saturated (single-domain) state is the equilibrium (minimum-energy) configuration of cellular patterns in the regime $H_B > H_{RI}$, and the equilibrium average cell area should therefore diverge as $H_B \to H_{RI}$. As shown in Fig. 10, for fixed H_B the tension grows as the domain spacing decreases, and the tension in cellular patterns of finite density is larger than the tension in an isolated stripe. We conclude that stripe segments in cellular patterns observed at bias fields $H_B > H_{RI}$ are under positive tension, and that such patterns are not in equilibrium.

We do, in fact, observe cellular patterns to persist into the nonequilibrium regime $H_B > H_{RI}$. As in the stripe array example of Fig. 10, a bias increment induces tension in the stripe segments that constitute the cell walls. In cellular patterns, a reduction in cell density is the mechanism by which the average domain spacing is increased and the tension thereby reduced. However, as we show in Sec. VI, the topological evolution is often obstructed by pentagonal bubble traps which resist elimination. In contrast to disordered stripe patterns, a reduction of cell

density sufficient to eliminate the tension cannot be achieved, and nonequilibrium cell patterns result. Our observation that the stripe segments do not buckle in response to bias field cycles of small amplitude for $H_B > H_{RI}$ supports the conclusion that all stripes are under positive tension in this regime.

A model of cellular domain patterns which parallels that of the stripe array could be pursued by appropriate alterations of the stray field expressions given above. The finite length of the stripe segments may be accounted for in this way, and further additions could include the stray fields originating in vertices and bubble traps, and perhaps incorporate disorder. The stripe energy would in general vary with position along its length, as it certainly does in real patterns, and the tension could be defined by examining the dependence of this energy on changes in the local pattern configuration. However, useful results are difficult to obtain, and we instead turn to the properties of the other elemental domain structures.

V. VERTICES

Threefold vertices play two key roles in the evolution of cellular patterns. First, vertex propagation favored by stripe tension reduces the total stripe segment length and leads to the elimination of cells. Second, the saturation bias field, i.e., the value of H_B at which all reversed magnetization disappears, occurs when the stripes are severed near the vertices, thereby destroying the connectivity of the patterns.

Vertices propagate when the tug of war between the tension in the adjoining stripe segments is unbalanced. For example, each of the two vertices in the photographs of Fig. 12 experiences a net effective force in the direction of the angles between the stripes which are less than 120°. The total stripe length and energy are reduced as the vertices "reel in" the stripes in the direction of advance and "reel out" a single stripe behind, with velocities indicated in the figure. Vertex velocity increases with net force, which increases with tension and with asymmetry in the local angles. As shown in Fig. 12, vertices observed in cellular patterns eventually attain stationary states with 120° vertex angles. We have observed individual vertices in very sparse patterns to propagate distances up to 1 cm before stopping.

Motion of the adjoining stripes necessarily accompanies vertex propagation. In Fig. 12, the portions of the "leading" stripes which are immediately adjacent to the vertices must move laterally to keep pace with the vertex. Vertex motion is opposed by coercive drag that acts predominantly on these laterally moving portions, and the velocities are apparently determined by a balance between this drag and the net force on the vertex due to tension and asymmetry. For fixed H_B, an increase in the amplitude H_{ac} of an ac field component increases the effective vertex mobility. For various combinations of the bias fields and tensions, vertex angles, and ac amplitudes, we have observed vertex velocities in the range ~ 1 to ~ 100 μm/s. In some cases, the direction of motion can be reversed by reducing H_B to produce negative stripe tension which favors an increase in stripe length. However, we have observed only small "negative" velocities (< 5 μm/s), because the dominant response to large negative tension is stripe buckling rather than vertex motion.

The motion of vertices leads to the collapse and elimination of cells, the dominant mechanism by which cellular patterns increase the average domain spacing and reduce tension in the stripe segments. Because the interior angles of cells with fewer than six sides are on average smaller than 120°, the shrinkage of these cells reduces the total stripe length and energy. Cell elimination therefore obeys the well-known topological selection rule[13] that favors the collapse of cells with fewer than six sides; the photographs in Fig. 13 show the collapse of a four-sided

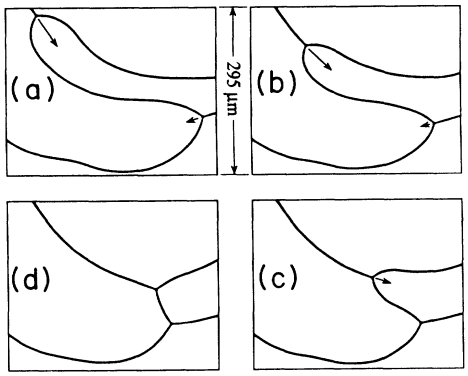

FIG. 12. Photographs showing vertex propagation at $H_B = 0.48 \times 4\pi M = 92$ Oe, with relative velocities indicated by the arrows. In frame (a), the velocity of the faster vertex is approximately 20 μm/s. Time intervals between successive frames increase through the sequence. The final, stationary state in frame (d) is characterized by zero net force on the vertices. An ac field ($H_{ac} = 3$ Oe, $\nu = 40$ Hz) is present throughout.

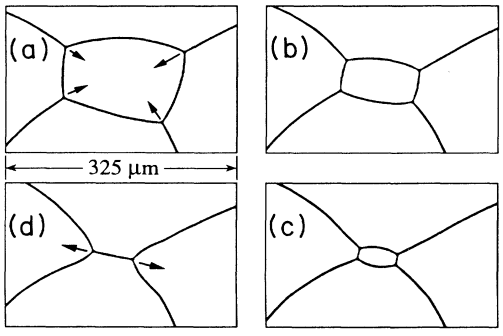

FIG. 13. Photographs showing the collapse of a four-sided cell. Bias is fixed at $H_B = 0.51 \times 4\pi M = 97$ Oe. The initial state in frame (a) is unstable due to tension in the stripe segments, and the vertices and segments accelerate as the cell collapses. The two remaining vertices in frame (d) seek positions of zero net force. An ac field ($H_{ac} = 4$ Oe, $\nu = 40$ Hz) is present throughout.

cell. The initial state is destabilized by an increment in H_B that creates tension in the stripe segments. The vertices and segments move cooperatively to reduce the stripe length, and domain motion ceases only after the cell has collapsed and the remaining two vertices have reached positions of zero net force. As the stripe segments that form the cell boundaries shorten, the interior vertex angles decrease, and the collapse accelerates.[22] With a sufficiently large ac component, the motion is smooth and visually identical to the contraction of soap bubbles.[13,14] Although the collapse of Fig. 13 momentarily brings the cell walls nearer to one another, the net result is an increase in the average domain spacing, and the tension in the stripe segments is reduced. The topological result of Fig. 13 is the elimination of the cell, two vertices, three stripe segments, and of one side from each of two neighboring cells. Such topological changes are irreversible: we have never observed a subsequent reduction in H_B to reconstruct a cell. We have also never observed $T1$ processes (see Ref. 13) which rearrange a local cell neighborhood but conserve the total numbers of sides, cells, and vertices. Three-sided cells collapse in a manner similar to Fig. 13.[23] However, we show in Sec. VI that the collapse of five-sided cells is often hindered by the formation of a stable bubble trap.

For $H_B < H_{RI}$, stable three- and four-sided cells are common in the stationary states, indicating that tension is zero in at least some of the stripe segments in this bias regime. In contrast, all segments are under tension if $H_B > H_{RI}$, and three- or four-sided cells formed in the course of the evolution are energetically unstable. If coercivity is mitigated by an ac field, these cells immediately collapse, and pentagonal bubble traps and irregular five-sided cells are the only cells with fewer than six sides that survive. Three- or four-sided cells are extremely rare for $H_B > H_{RI}$, except in very sparse patterns where coercivity dominates (Sec. VII).

The photographs in Fig. 14 show that the stripes are pinched near the vertices. The pinching occurs because the vertex center experiences the demagnetization field of three semiinfinite stripes, which is significantly greater than the self-field H_D^{self} of an isolated stripe. The bias field in the second frame is larger than in the first, and the stripe widths are greatly reduced. The width of the pinched region approaches zero as H_B nears a critical value H_V; one or more stripes are severed, and the vertex

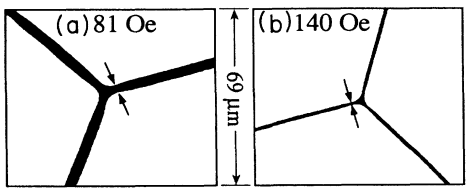

FIG. 14. Photographs of stationary vertices at two bias values. Both the minimum widths of the pinched regions (arrows) and the stripe widths far from the vertices decrease as H_B increases. The stripes are severed and the vertices destroyed at $H_V = 0.79 \times 4\pi M = 150$ Oe.

is destroyed. The adjoining stripe segments are under tension, and a severed stripe runs back along its length very rapidly, like a broken rubber band. We have observed this pinch-off only in extremely sparse cellular patterns, at a bias value $H_V = 0.79 \times 4\pi M = 150 \pm 1$ Oe, as determined experimentally by averaging the results of several sweeps of H_B from initial ($H_B = 0$) bubble seas. All vertices and stripe segments are simultaneously eliminated, and H_V thereby determines the saturation bias field for cellular patterns. Cellular patterns persist to significantly larger bias fields than any other domain patterns observed in low-defect garnets. The next largest[7] saturation field is that of nonequilibrium bubble lattices, which persist to the magnetic bubble collapse field[1,3,5] $H_{col} = 0.53 \times 4\pi M = 101$ Oe.

VI. PENTAGONAL BUBBLE TRAPS

The final domain structure that we consider is the pentagonal bubble trap shown in the lower photographs of Fig. 15. Five stripe segments separated by nearly equal angles are connected at the central body. Contained inside is a circular domain of magnetization aligned with H_B, opposite to the reversed magnetization that comprises conventional magnetic bubbles. Bubble traps begin to form at bias fields a few oersteds less than the run-in field, and comprise a significant fraction of all cells throughout their range of stability.

As shown in Fig. 15, bubble traps are formed via the contraction of five-sided cells. In this example, $H_B > H_{RI}$, and tension in the stripe segments initiates a collapse similar to that of the four-sided cell in Fig. 13. The inner domain of up magnetization is squeezed down to the circular bubble as the cell shrinks, and the bubble trap is formed. The bubble acts as a barrier to further collapse, and the bubble trap is not destroyed. Its struc-

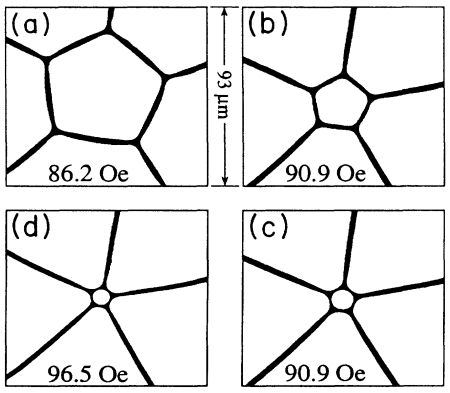

FIG. 15. Photographs showing the formation of a pentagonal bubble trap. The stable five-sided cell in frame (a) is destabilized by an increase in H_B. The collapse halts when the stable bubble trap in frame (c) is formed. The bubble trap shrinks slightly but resists total collapse when H_B is increased further [frame (d)]. An ac field ($H_{ac} = 3$ Oe, $\nu = 40$ Hz) is present throughout.

ture is robust in that a further, significant increase in the bias field only slightly shrinks the bubble trap [frame (d) of Fig. 15].

The formation of bubble traps is irreversible in sparse patterns for $H_B > H_{RI}$. Subsequent reduction of H_B does not reverse the sequence of Fig. 15, but instead results in stripe buckling if H_B is reduced much below H_{RI} (see, for example, Fig. 4). In denser patterns the shorter stripe segments buckle less easily, and pentagonal traps can sometimes be "reinflated" by producing negative tension in the segments.

The bubble traps are mobile, but propagation is less common than that of threefold vertices. A trap moves as a coherent structure, driven again by tension in the five attached stripes. The velocities are typically smaller (<5 μm/s) than that of vertices, which may be due to smaller net forces on the bubble traps, or to lower mobility of the complex structure of the trap and of the greater number of attached stripes.

Sufficient increase of H_B results in the sudden destruction of a given bubble trap, as shown in the photographs in Fig. 16. The fivefold vertex which remains after the collapse is highly unstable, and immediately disassembles into threefold vertices. If $H_{ac}=0$, the collapse of an isolated bubble trap occurs at a bias field $H_5=0.54\times 4\pi M=103\pm 1$ Oe, as determined experimentally by averaging the results of several increasing sweeps of H_B. We have observed individual bubble traps to survive over the entire range of applied field $H_{RI}<H_B<H_5$, an interval of $0.10\times 4\pi M=19$ Oe. The topological results of the collapse are also shown in Fig. 16: one of the neighboring cells gains one side, two cells each lose one side, and the remaining two are unchanged. The Euler requirement that the average number of cell sides be 6 (Ref. 13) is preserved. We have not found any criteria that can realiably predict the orientation of the collapse, i.e., which neighbor gains a side.

The destruction of bubble traps appears to be triggered by a collapse of the enclosed bubble analogous to that observed for conventional magnetic bubbles.[1,3,5] Both H_B and the demagnetization field component originating in the reversed magnetization favor the expansion of the bubble, while the domain-wall energy and the demagnetization field of the up magnetization outside the trap favor its collapse. (The roles of the bias field and demagnetization field are reversed relative to the conventional bubble case.) An increase in H_B reduces the amount of reversed magnetization, as can be seen in the lower frames of Fig. 15. At a critical bias value and bubble radius, the influences of the wall energy and the up demagnetization field dominate, and the trap collapses. As with conventional bubbles,[1,3,5] it is likely that the stable bubble radius at bias fields below the collapse point is determined by a local minimum in the bubble energy versus radius, and that the collapse corresponds to the elimination of this local minimum. This conjecture is supported by numerical estimates of the bubble energy in a simplified model geometry. Furthermore, we observe fluctuations in the bubble radius of up to $\sim 25\%$ just prior to collapse in response to an ac field (~ 1 Oe amplitude, 10–20 Hz). The fluctuations suggest a weak dependence of bubble energy on radius, consistent with the disappearance of a local energy minimum at collapse.

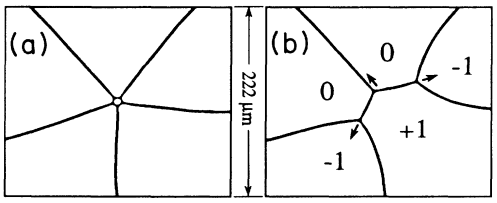

FIG. 16. Photographs showing the destruction of a pentagonal bubble trap via collapse of the bubble; $H_B=0.51\times 4\pi M=97$ Oe. The fivefold vertex which remains is unstable and immediately disassembles into stable threefold vertices [frame (b)] that seek positions of zero net force. The neighboring cells gain or lose sides as indicated. An ac field ($H_{ac}=2$ Oe, $\nu=40$ Hz) is present throughout. The bubble trap collapses at $H_B<H_5=103$ Oe in this example because the stray fields of other reversed domains (beyond the visible region) and the ac field both add to the influence of H_B.

The pattern evolution and stationary states are particularly interesting in the "high-tension" bias regime $H_{RI}<H_B<H_5$. Because all stripe segments are under tension in this regime, three- and four-sided cells are unstable, and are rarely observed in the stationary patterns if an appropriate ac field is applied. The patterns energetically factor saturation by the successive elimination of all cells and a corresponding divergence in cell area at $H_B=H_{RI}$. However, the robust bubble traps obstruct the topological evolution, and cellular patterns observed in the high-tension regime are far from energetic equilibrium. The bubble traps visibly support the stationary patterns, as can be seen in Fig. 2. As the only stable cells with fewer than six sides, they also provide the topological balance necessary to keep the averge number of sides equal to 6. We observe that the average cell area diverges only as $H_B\rightarrow H_5$ and all bubble traps are destroyed. (As will be discussed in Sec. VII, a few cells persist beyond H_5 due to coercive drag on the very long stripe segments.) Furthermore, although the cell density continuously decreases as H_B increases, we find that the fraction f_5 of total cells which are bubble traps in the stationary states satisfies $f_5\approx 0.20$ throughout the bias range $H_{RI}<H_B<H_5$, and drops abruptly to zero at $H_B=H_5$. Within this range, the condition for collapse of an individual bubble trap depends upon H_B and the domain configuration, i.e., the extent to which the stray fields enhance H_B at the bubble trap location. Finally, we observe very long settling times of up to several minutes after the collapse of a bubble trap destabilizes a stationary configuration. The collapse triggers a chain reaction in which subsequent domain motion results in the collapse of a series of bubble traps and other cells.

VII. COERCIVE EFFECTS AND THE ac FIELD

Coercivity strongly affects the evolution of cellular and stripe patterns, and can significantly alter the geometry,

topology, and energy of the stationary states. In characterizing the pattern evolution it is essential to distinguish between behavior dictated by energetics, which we have focused on thus far, and that determined by coercive drag. In this section we describe the coercive effects and the extent to which an ac field component can mitigate them while leaving the one-parameter (H_B) nature of the evolution intact.

The stationary cellular pattern shown in the photograph in Fig. 17 was produced by slowly increasing H_B from zero with no ac field component present. It is apparent that this configuration has not attained a local energy minimum. Some stripe segments have large and even serpentine curvatures, even though they are under tension, and domain motion is prevented by coercive friction in many of the smaller cells that energetically favor collapse. The vertices themselves are nonetheless in equilibrium: the local angles are all nearly 120°. Large bias increments (>10 Oe) and correspondingly large stripe tensions are typically required to break free domains stuck by coercivity. The subsequent domain velocities are momentarily very large ($\gg 100$ μm/s), and the settling times required to reach a new stationary state are small (<1 s). The evolution under slowly increasing bias proceeds by a series of sudden ruptures in which several cells in close proximity are simultaneously destroyed. Stripe segments that constitute the cell walls are frequently severed in the process, and the elimination of cells by continuous shrinkage (as in Fig. 13) is often bypassed. The wall severing in the absence of an ac field is anomalous in that it does not appear to be caused by a continuous pinch-off such as occurs with the vertices as discussed above, and it usually occurs during points in the evolution at which the domain velocities are large. Topologically, the severing of a wall merges two cells and often results in cells with many sides;[24] the largest (partially obscurred) cell in Fig. 17 has more than 20 neighbors.

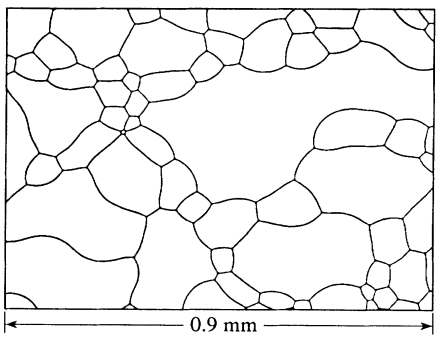

FIG. 17. Photograph of a cellular pattern evolved from a homogeneous bubble sea to $H_B = 0.52 \times 4\pi M = 99$ Oe with no ac-field component. Many effects of coercivity are apparent, including large stripe curvature in spite of tension, and large cells with many neighbors formed by cells merging when stripe segments are anomalously served. Cells with fewer than six sides energetically favor collapse, but domain motion is prevented by coercive friction.

A coercivity-dominated configuration such as in Fig. 17 responds to the application of an ac field by the straightening of stripe segments and the collapse of several cells. The configuration energy is reduced, and the stationary state eventually reached is characterized by stripe tensions which are balanced at the vertices and bubble traps; see, for example, Fig. 2. The ac component thereby aids the domains in attaining metastable configurations which are not dominated by coercive pinning. Furthermore, the domain motion with ac present is typically smooth, and we find that the anomalous stripe severing described above can be avoided in the Airtron garnet if the amplitude and frequency are chosen appropriate.[25] The topological evolution proceeds by the orderly elimination of cells by collapse, and cells with more than 12 sides are extremely rare. In the bias regime $H_{RI} < H_B < H_5$, the observed stationary configurations are not in equilibrium, whether or not an ac component is present. However, with coercive effects mitigated by an ac field, the patterns correspond to local energy minima, and energy barriers in the form of bubble traps obstruct the topological evolution and prevent the patterns from reaching equilibrium. In contrast, in the absence of an ac field, the evolution is inhibited primarily by coercive friction. For these reasons, we have found the ac field essential in our attempt to characterize cellular evolution.

We have found that the ac amplitude H_{ac} required to overcome coercive effects is much larger than the coercive field H_c which acts on the individual domain walls. A large ac amplitude is necessary because stripe tension produces only a small motive force, as described below. Consider a stripe segment with local radius of curvature r_s much greater than the stripe width w_s. As described in Sec. III, stripe tension $T_s > 0$ results in a pressure $P_s = T_s / r_s$ acting normal to the stripe which favors a reduction in curvature, with a corresponding reduction in length and increase in r_s. Opposing P_s is the effective coercive pressure $P_c = 4MtH_c$, which is the sum of the coercive pressures on both domain walls. The condition $P_s > P_c$ must be met before the stripe responds by increasing r_s. The view that these pressures act on the stripe domain as a whole, as opposed to the domain walls individually, is justified by the strong constraints on the stripe width w_s described in Sec. III.

An estimate of an appropriate ac amplitude H_{ac} can be obtained by considering the response of a curved stripe segment to changes in the bias field. If H_B is set so that $T_s = 0$, then superimposing an ac field will modulate T_s and the pressure P_s around zero, as illustrated in Fig. 18(a). The ac field tugs on the stripe repeatedly as the tension passes through its maximum T_s^{max}. The condition which we impose is that H_{ac} be sufficiently large that the maximum lateral pressure P_s overcomes the coercive pressure P_c. The stripe will then break loose at the cycle maximum and decrease the curvature. (Only for excessively large H_{ac} have observed stripe segments to buckle at the cycle minimum). For a local radius of curvature r_s, this criterion for H_{ac} is equivalent to $T_s^{max}/r_s = P_c$. We can evaluate H_{ac} for the particular case of an isolated stripe and $H_B = H_{RI}$; the condition then becomes

$E_s(H_{RI}+H_{ac})/r_s=4MtH_c$. Figure 18(b) shows this relation expressed as the minimum radius r_s^{min} not affected by H_{ac} plotted versus H_{ac} where we have set $H_c=0.25$ Oe and used the values $T_s=E_s$ determined for the isolated stripe in Sec. III. The radius r_s^{min} corresponds to the maximum curvature expected in the stripe segment versus H_{ac}. Note that an amplitude of several oersteds is required to increase the minimum radius to the $r_s>50$ μm range typical of medium- to low-density patterns. Figure 18(b) thus agrees with our observations that H_{ac} must be several times larger than H_c in order to overcome coercive friction on the motion of stripe segments. Figure 18(b) also applies approximately to stripes of zero tension embedded in patterns, because the slope of T_s versus H_B near the zero crossings of Fig. 11 does not depend strongly on spacing.

Furthermore, Fig. 18(b) can be used to estimate the expected minimum radius of stripe curvature in cases where H_B is such that the stripe tension is positive without an ac field. The minimum curvatures r_s^{min} are in general determined by $T_s(H_B+H_{ac})/r_s=4MtH_c$. For given H_{ac}, r_s^{min} can be evaluated for an isolated stripe by a horizontal shift of the curve in Fig. 18(b) of magnitude $H_B=H_{RI}$, with the result that r_s^{min} increases with H_B. We observe this dependence in sparse stripe patterns and in cellular patterns. For any fixed H_{ac}, the maximum observed curvature slowly decreases with H_B. Note that in the high-bias regime $H_B>H_5$, cellular patterns energetically favor the reduction of total stripe length toward zero and the successive elimination of all cells, and there are no bubble traps to obstruct the evolution. However, because r_s^{min} is finite for any H_B and H_{ac}, coercive drag prevents the collapse of large cells, and the pattern survives to $H_B=H_V$.

Even with an adequate ac amplitude, coercive effects on the evolution are significantly reduced for only a limited range of ac frequency ν. The response of the domains to the ac field (as measured, for example, for the observed r_s^{min} for fixed H_B and H_{ac}) falls off monotonically with frequency ν from dc, and the above determinations of H_{ac} underestimate the required amplitude. We find that the ac field has no significant influence on the domain motion for frequencies $\nu\gtrsim 200$ Hz. This cutoff is surprisingly small in light of the "fast" times associated with the effective domain wall "mass."[5] For example, resonant frequencies of domain-wall oscillations in parallel stripe patterns have been measured in the range 10–100 MHz.[26] The cutoff at 200 Hz may originate in the interplay of the coercive pressure on the domain walls and the demagnetization feedback that constrains the relative wall positions within small limits. However, we do not fully understand this effect.

In addition to affecting the dynamics of the stripe segments, the ac field also alters the bubble trap collapse fields. The traps collapse when the ac field swings high, and the corresponding measured values of the bias fields decrease as H_{ac} increases. For example, the amplitude and frequency dependence of the collapse field H_5 of an isolated bubble trap have the approximate form $H_5=H_5^0-C(\nu)H_{ac}$, where $C(\nu\to 0)=1$ and $C(200\ \text{Hz})\approx 0$, with monotonic decrease between. ac fields of useful amplitude can alter the bubble trap collapse field H_5 by several Oe. Surprisingly, we find that the ac field shifts the vertex instability and corresponding saturation at H_V by less than 1 Oe.

These observations indicate that, in spite of its beneficial influence on the pattern evolution, the ac field can only partially eliminate the effects of coercivity. Increasing H_{ac} overcomes coercive effects on stripes of increasingly smaller curvature, but alters the bubble collapse bias field H_5 and thereby interferes with the pattern evolution. A useful compromise is nonetheless possible so that the ac amplitude and frequency can be fixed, and the evolution then studied as a function of H_B alone. We have found that the configuration with $\nu=40$ Hz and H_{ac}7.5 Oe has several desirable features which hold over the entire bias range $0<H_B<H_V$: dynamic response of the patterns to small bias increments ($\ll 1$ Oe), uniformly smooth domain motion, and severing of stripe segments, that occurs only very infrequently and only at large bias values near H_V.

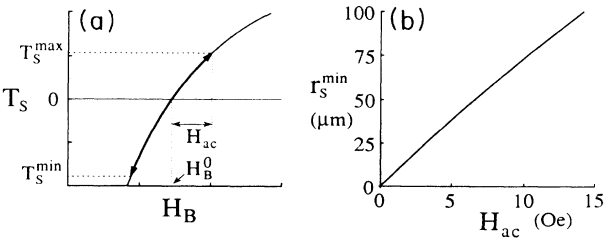

FIG. 18. (a) Modulation of stripe tension by an applied ac field (arbitrary units). In this example, H_B is set so that the tension is zero at midcycle. (b) Critical radius of stripe curvature vs ac-field amplitude as calculated for an isolated stripe and $H_B=H_{RI}$. The tension at the ac cycle maximum is sufficient to preclude local curvature radii $r_s<r_s^{min}$.

VIII. DISCUSSION AND CONCLUSIONS

A synthesis of the properties of the stripe segments, vertices, and bubble traps described above gives an overall picture of the evolution of cellular domain patterns in garnet films from an initial ($H_B=0$) disordered bubble sea. A pattern is stationary when H_B is fixed, but is destabilized by an increment in H_B, and motion of the domains ensues as the pattern seeks a new stationary state. The bias field thus serves as a control parameter which generates a sequence of stationary states when it is monotonically increased in small intervals. Tension in the stripe segments drives the domain motion and accounts for most of the excess energy in nonequilibrium patterns, i.e., the energy in excess of that in minimum-energy configurations. For fixed H_B, tension is reduced

by increasing the average domain spacing, thereby reducing the influence of the stray fields on a given stripe segment. Toward this end, the domain dynamics reduce the total stripe segment (cell wall) length and attempt to eliminate cells with fewer than six sides. The stripe run-in field H_{RI}, the vertex pinch-off field H_V, and the bubble trap collapse field H_5 delineate the various bias regimes that characterize the overall evolution. If an appropriate ac field is applied, coercive effects are minimized and the stationary states are (approximately) metastable. The bias regimes are then characterized as follows.[27]

(i) $H_B < H_{RI}$. The patterns are able to eliminate cells as needed to maintain nearly zero stripe tension, and the stationary states remain close to energetic equilibrium. Settling times in the seeking of stationary states are generally very small.

(ii) $H_{RI} < H_B < H_5$: the "high-tension" regime. The rate of cell elimination (versus bias increase) is high; the cell density drops more than two decades in this regime. The saturated state is the equilibrium configuration, and all stripe segments are under tension. However, stable bubble traps obstruct the topological evolution and support nonequilibrium configurations. An increment in H_B destabilizes and collapses certain bubble traps, and triggers "chain reactions" in which subsequent domain motion results in the collapse of a series of bubble traps before a stationary state is reached. Long settling times (up to several minutes) are typical, even when the bias increments are small (< 1 Oe). The dynamics of these adjustments are visually similar to those of soap films. Metastable patterns are characterized by segment tensions balanced at the vertices and bubble traps. Except for a few cells which remain due to coercive drag on the long cell walls, the average cell size diverges at $H_B = H_5$ when the last bubble traps collapse.

(iii) $H_5 < H_B < H_V$. The patterns are extremely sparse, and coercive drag on the stripe segments prevents the successive elimination of the remaining cells that is favored energetically. All reversed domains are eliminated and the garnet saturated at $H_B = H_V$ when the vertices are destroyed.

Although coercive effects can be partially suppressed with an ac field, this is achieved at the expense of altering the boundaries of the above regimes. The strongest influence is on the value of H_5: increasing H_{ac} effectively reduces H_5 and "squeezes" the high-tension regime, although the behavior within it does not change significantly.

Cellular domain patterns share many features with other two-dimensional cellular systems that are driven by surface tension to disorder topologically. Of these, the two-dimensional soap froth is the simplest, and has been studied[12,13,28] as a prototype for coarsening in polycrystalline materials[15,16] and other systems. In spite of simple local dynamics of individual cells in the idealized system, the overall behavior of the soap froth is very subtle. Recent experimental[14,29] and theoretical[30–33] efforts and computer simulations[34,35] have made progress on the issues of scaling states[36] and of correlations between probability distributions of cell characteristics, but leave them incompletely resolved. Furthermore, results of recent experiments[14,29] concerning the rate of coarsening disagree with older results[12] and with theoretical predictions,[33] and indicate that small deviations in the experimental system from the idealized model can strongly affect the overall evolution.

The analogy between the cellular domain patterns and soap froths is grounded in the stripe tension that drives the evolution. If the ac field is chosen appropriately, the increase in disorder has the same topological character as the soap froths, in that cells with fewer than six sides are preferentially eliminated. The energetics that govern the domain evolution are, however, more complex than those of soap froths. The nature of the evolution depends on the bias regime, in contrast to the time-invariant dynamical rules that govern the idealized soap froth. in addition, the stripe tension is not uniform, but varies with local domain configuration, and soap froths have no analog of the bubble traps to obstruct the topological evolution. Coercivity and the application of an ac field to mitigate its effects further complicate matters.

In spite of its complexity, many features of the cellular domain system are experimentally desirable. If the ac field is fixed, the evolution is easily controlled by the single parameter H_B. The stationary states can be studied at leisure, and the motion of the domains as the patterns seek these states can in some cases be temporarily stopped by removing the ac field. Furthermore, it is a large system: the initial ($H_B = 0$) state contains several million bubbles, and the boundary effects that typically affect soap froth experiments and simulations may be avoided over a wide bias range.

Another useful feature of the cellular domain system is that the degree of order in the initial ($H_B = 0$) can be varied by "annealing" a disordered bubble sea.[9] If the initial state is highly ordered in the form a "granular" triangular bubble lattice, the evolution under increasing bias proceeds by a "melting" transition, as shown in Fig. 1. A sufficient increase in H_B creates a stressed hexagonal cellular lattice with tension in the stripe segments in a manner analogous to the frothlike evolution described above. However, the symmetry of the ordered lattice precludes evolution via vertex motion and cell collapse, except at topological defects and grain boundaries where cells with other than six sides are located. The evolution is thus not homogeneous as in the case of the frothlike evolution described above. Instead, a front which is nucleated at the defects separates the hexagonal lattice from a disordered frothlike region. As shown in Fig. 1, the motion of the front is mediated by the collapse of the bubble traps which line its length, and it irreversibly advances and destroys the lattice.

In conclusion, cellular domain patterns in garnet films constitute a rich and accessible cellular system. In the high-tension bias regime, the evolution produces a complex sequence of metastable states with unusual topological constraints imposed by the instability of three- and four-sided cells, and interesting dynamics and long settling times arise as the patterns seek these states. The divergence of average cell area at $H_B = H_5$ is unique

among cellular systems; arbitrarily large cell area corresponds to infinite time in the soap froth, and, to our knowledge, no other cellular systems show analogous behavior at finite control parameter. Finally, an ordered initial state results in an irreversible, stress-induced "melting" transition, with an interesting dependence on bias field and cell density. We plan to pursue these topics in greater detail in forthcoming papers.

ACKNOWLEDGMENTS

We thank Raymond Wolfe for helpful discussions, and Roger Belt and the Airtron Division of Litton Industries for supplying the garnet sample. Raj Seshadri's help with the computer analysis is also gratefully acknowledged. This work was supported by the Office of Naval Research under Contract Nos. N00014-84-K-0329 and N00014-84-K-0465.

[1]A. H. Eschenfelder, *Magnetic Bubble Technology* (Springer-Verlag, New York, 1981).

[2]T. H. O'Dell, Rep. Prog. Phys. **49**, 589 (1986).

[3]A. A. Thiele, Bell Syst. Tech. J. **48**, 3287 (1969).

[4]A. A. Thiele, A. H. Bobeck, E. Della Torre, and U. F. Gianola, Bell Syst. Tech. J. **50**, 711 (1971).

[5]A. P. Malozemoff and J. C. Slonczewski, *Magnetic Domain Walls in Bubble Materials* (Academic, New York, 1979).

[6]C. Kooy and U. Enz, Philips Res. Rep. **15**, 7 (1960).

[7]J. A. Cape and G. W. Lehman, J. App. Phys. **42**, 5732 (1971).

[8]W. F. Druyvesteyn and J. W. F. Dorleyn, Philips Res. Rep. **26**, 11 (1971).

[9]G. R. Woolhouse and P. Chaudhari, Philos. Mag. **31**, 161 (1974).

[10]P. Molho, J. Gouzerh, J. C. S. Levy, and J. L. Porteseil, J. Magn. Mater. **54-57**, 857 (1987).

[11]D. Sornette, J. Phys. (Paris) **48**, 151 (1987).

[12]D. A. Aboav, Metallography **13**, 43 (1980).

[13]Review of cellular systems: D. Weaire and N. Rivier, Contemp. Phys. **25**, 59 (1984).,

[14]J. A. Glazier, S. P. Gross, and J. Stavans, Phys. Rev. A **36**, 306 (1987).

[15]S. K. Kurtz and F. M. A. Carpay, J. Appl. Phys. **51**, 5725 (1981).

[16]M. P. Anderson, D. J. Srolovitz, G. S. Grest, and P. S. Sahni, Acta Metall. **32**, 783 (1984); **32**, 793 (1984).

[17]R. F. Belt and J. B. Ings, SPIE J. **753**, 142 (1987).

[18]C. Kittel, Rev. Mod. Phys. **21**, 541 (1949).

[19]The overall effect differs from the pseudothermal agitation of magnetic bubble lattices by an ac field in which the bubbles jiggle randomly around their equilibrium positions (Ref. 9).

[20]A. H. Bobeck, Bell Syst. Tech. J. **46**, 1901 (1967).

[21]Equilibrium here refers to the minimum energy attainable by the stripe array for fixed H_B. For certain bias fields, minimum-energy bubble lattices have lower energy than the minimum-energy stripe patterns (Ref. 7), and are therefore the *global* equilibrium domain configurations for these bias values. However, the energy barriers between these two classes of patterns are large at room temperature, and transitions between them are not observed.

[22]Although the vertices and cell walls accelerate, the rate of change of the area of a given cell remains more nearly constant. This behavior is qualitatively similar to Von Neumann's laws governing the dynamics of idealized soap bubbles and metal grains [Refs. 13 and 14, and J. Von Neumann, in *Metal Interfaces*, edited by C. Herring (American Society for Metals, Cleveland, 1952), p. 108], which predicts that the rate of change of the cell area is proportional to $n-6$, where n is the number of sides, and is independent of the area itself.

[23]We observe two-sided "cells" only when the ac field is absent and coercivity dominates the patterns.

[24]The merging of two cells with n_a and n_b sides results in a cell with $n=n_a+n_b-4$ sides.

[25]In other garnets we have examined, the ac field is also beneficial, but does not completely eliminate stripe severing that sometimes occurs in conjunction with large stripe tension and the collapse of four-sided cells.

[26]B. E. Argyle, W. Jantz, and J. C. Slonczewski, J. Appl. Phys. **54**, 6 (1983).

[27]We omit the regime $H_B \lesssim 0.26\times 4\pi M = 50$ Oe in which the pattern is a bubble sea rather than a cellular pattern with distinct cell walls and vertices.

[28]C. S. Smith, in *Metal Interfaces*, edited by C. Herring (American Society for Metals, Cleveland, 1952), p. 65.

[29]J. Stavans and J. Glazier, Phys. Rev. Lett. **62**, 1318 (1989).

[30]N. Rivier, Philos. Mag. B **52**, 795 (1983).

[31]C. W. J. Beenaker, Phys. Rev. Lett. **57**, 2454 (1986).

[32]M. Marder, Phys. Rev. A **36**, 438 (1987).

[33]C. W. J. Beenaker, Physica **147A**, 256 (1987).

[34]J. Wejchert, D. Weaire, and J. P. Kermode, Philos. Mag. B **53**, 15 (1986).

[35]D. Weaire and J. P. Kermode, Philos. Mag. B **48**, 245 (1983); **50**, 379 (1984).

[36]D. Weaire and J. P. Kermode, Philos. Mag. B **47**, L29 (1983).